Supporting information

for

Electronically delocalized Ir enables stable and efficient acidic water splitting

Hao Hu[a]‡, Farhad MD Kazim[a]‡, Zihao Ye[a], Yuhua Xie[a], Quan Zhang[a], Konggang Qu[b], Jingxiang Xu[c*], Weiwei Cai[a*], Shenglin Xiao[a] and Zehui Yang[a*]

[a]Sustainable Energy Laboratory, Faculty of Materials Science and Chemistry, China University of Geosciences Wuhan, 388 Lumo RD, Wuhan, 430074, China

[b]Shandong Provincial Key Laboratory/Collaborative Innovation Center of Chemical Energy Storage & Novel Cell Technology, Liaocheng University, Liaocheng, 252059, China.

[c]College of Engineering Science and Technology, Shanghai Ocean University, Shanghai 201306, China.

Hao Hu and Farhad MD Kazim equally contributed to this work.

Experimental section

Materials: Chloroauric acid (HAuCl$_4$·4H$_2$O), hydroxylate multi-walled carbon nanotubes, iridium (III) trichloride (IrCl$_3$, 99.95%) and iridium (IV) oxide (IrO$_2$, 99.9%, metals basis) were purchased from Aldrich Chemical. Ethylene glycol and ethanol were purchased from Sinopharm Chemical Reagent Co., LTD. Nafion solution (5 wt%) and 20 wt% Pt/C was obtained from Alfa Aesar. The water used in all experiments was deionized water (DIW). All chemicals were used as received without further purification.

Material characterization: The morphologies and structures were characterized by field-emission scanning electron microscopy (SEM, Hitachi SU8010) and transmission electron microscopy (TEM, Tecnai G2 F20). The crystal structure of the synthesized electrocatalyst was detected by X-ray diffraction (XRD, Bruker AXS D8-Focus, Germany) with Cu Kα radiation in the range of 2θ from 30° to 70°. X-ray photoelectron spectroscopy (XPS) was performed by using Thermo-Scientific K-Alpha equipment. Brunauer−Emment−Teller (BET) surface areas and pore size measurements were performed with N$_2$ adsorption/adsorption isotherms at 77 K on a Quantachrome Autosorb-iQ2 instrument. The amount of metals in the catalyst was calculated by the ICP-OES method using Perkin Elmer Optima 5300 DV. The Ir L$_3$-edge XAS spectra was carried in fluorescence mode in SPring-8. The acquired XAS data were processed according to the standard procedures using the ATHENA module implemented in the IFEFFIT software package and FEFF8.20.

Electrochemical measurements: Electrochemical measurements were conducted with Gamry (interface 1000E, USA) instrument at room temperature of 25°C. Electrocatalyst ink was prepared by dispersing freshly synthesized catalyst powder (2 mg) in a solution containing 800 µL of deionized water, 185 µL of isopropanol and 15 µL of Nafion solution (5 wt%) followed by ultrasonication for 2 h. Then 10 µL of the ink was cast on a glassy carbon electrode (GCE, diameter = 3 mm) to prepare a working electrode. All electrochemical experiments were carried out in a three-electrode glass cell with a carbon rod as the counter electrode and an Ag/AgCl as the reference electrode. The 0.5 M H_2SO_4 solution was used for the electrochemical electrolyte and the solutions were saturated with N_2 for 30 min prior to the HER or overall water splitting test or with O_2 prior to the OER test. The linear sweep voltammetry curves were recorded with a scan rate of 5 mV s^{-1}. CV was carried out with a scan rate of 50 mV s^{-1}. The electrochemical double-layer capacitance was measured at different scan rates from 10 to 100 mV s^{-1}. EIS was measured from 100 kHz to 0.05 Hz under AC voltage amplitude of 5 mV and DC voltage based at a given potential at 10 mA cm^{-2}. The long-term stability was measured by chronoamperometric (I-t) stability examination at a given potential. As for the water electrolysis, a two-electrode system was applied for the overall water splitting. The catalysts were first loaded onto GCE (loading: 0.285 mg cm^{-2}) and used as both the anode and cathode. All data were presented without iR compensation. All potential were converted to the

reversible hydrogen electrode (RHE) based on the equation: $E(RHE)=E(Ag/AgCl)+0.241+0.059*pH$. In this work, we assumed the pH was 0 for 0.5 M H_2SO_4 electrolyte. Turnover frequency (TOF) was calculated based on the following equation: $TOF_{catalyst}$ (s^{-1}) = i_0 (A cm^{-2}) / {[Density of Ir atoms in the catalyst (sites/cm^2)] x [1.602 x 10^{-19} (C/e^-)] x [2 e^-/H_2]}.

Computational details: All periodic density functional theory (DFT) calculations with spin polarization were performed by using the Vienna ab initio simulation package (VASP) with the Perdew−Burke−Ernzerhof (PBE) exchange-correlation functional. The projector-augmented plane wave (PAW) was used to describe the interactions between core electrons and ions. A plane-wave cutoff energy was tested and set to 400 eV in all calculations. 3×3×1 Monkhorst-Pack grid k-points are employed for geometric optimization, and the convergence threshold is set as 10^{-4} eV in energy and 0.02 eV/Å in force, respectively. To calculate the free energy diagram of the OER process and HER, we employ the model of Ir (111) and AuIr (111) $\sqrt{3} \times \sqrt{3}$ surfaces. A vacuum distance of 15 Å was imposed between neighboring slab images in order to avoid interactions between periodic images.

OER: The reaction free energy ΔG for oxygen evolution reaction (OER) is approximated as:

$\Delta G = \Delta E + \Delta ZPE - T\Delta S$,

where ΔE, ΔZPE, and ΔS are the different adsorption energy, zero-point energy, and entropy of the reaction, respectively. Here, the adsorption

energies of O*, OH*, and OOH* were calculated by

$\Delta E_{OH*} = E(OH*) - E(*) - (E_{H2O}-1/2E_{H2})$,

$\Delta E_{O*} = E(O*) - E(*) - (E_{H2O}-E_{H2})$,

$\Delta E_{OOH*} = E(OOH*) - E(*) - (2E_{H2O}-3/2E_{H2})$,

where $E(*)$, $E(OH*)$, $E(O*)$, and $E(OOH*)$ are the ground state energies of a Ir or IrAu surface, Ir or IrAu surface adsorbed with OH*, O*, and OOH*, respectively. E_{H2O} and E_{H2} are the calculated DFT energies of H_2O and H_2 molecules in the gas phase.

HER: The hydrogen adsorption free energies were calculated as:

$\Delta G_{H*} = \Delta E_{H*} + \Delta ZPE - T\Delta S$,

where $\Delta EH*$ is the hydrogen chemisorption energy. ΔZPE and ΔS are the zero-point energy difference and the entropy difference between the adsorbed and the gas phase, respectively. Here, the hydrogen chemisorption energy is defined by

$\Delta E_{H*} = 1/n\ (E(slab+nH) - E(Surf) - n/2\ E(H_2))$,

where n is the number of H atoms in the calculations, $E(slab+nH)$, $E(Surf)$, and $E(H_2)$ are the total energies of the adsorption of n H atoms, clean surfaces, and gaseous hydrogen molecule, respectively.

Table S1 Comparison of OER activities of Ir-based electrocatalysts tested in 0.5 M H_2SO_4 electrolyte.

Electrocatalyst	Ir loading (µg cm^{-2})	Overpotential@10 mA cm^{-2} (mV vs. RHE)	Ref.
$Au_{0.5}Ir_{0.5}$@CNT	14.3	257	this work
Ir-STO	54	247	[1]
Li-IrOx	50	290	[2]
Ru@IrOx	58	282	[3]
IrOx/ATO	10.2	440	[4]
Ir-Cu nanocrystals	60	310	[5]
IrPd nanocages	12.5	226	[6]
IrW/C	10.2	310	[7]
IrNi-RF	10.4	313.6	[8]
Ir nanosheets	200	240	[9]
Ir@Co_4N NFs	29	310	[10]
Co-RuIr	33	235	[11]
Ir WNWs	31	270	[12]
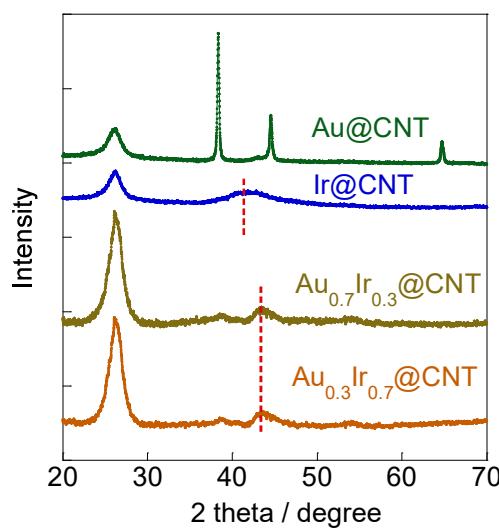
Figure S1 XRD patterns of Au@CNT, $Au_{0.3}Ir_{0.7}$@CNT, $Au_{0.7}Ir_{0.3}$@CNT and

Ir@CNT.
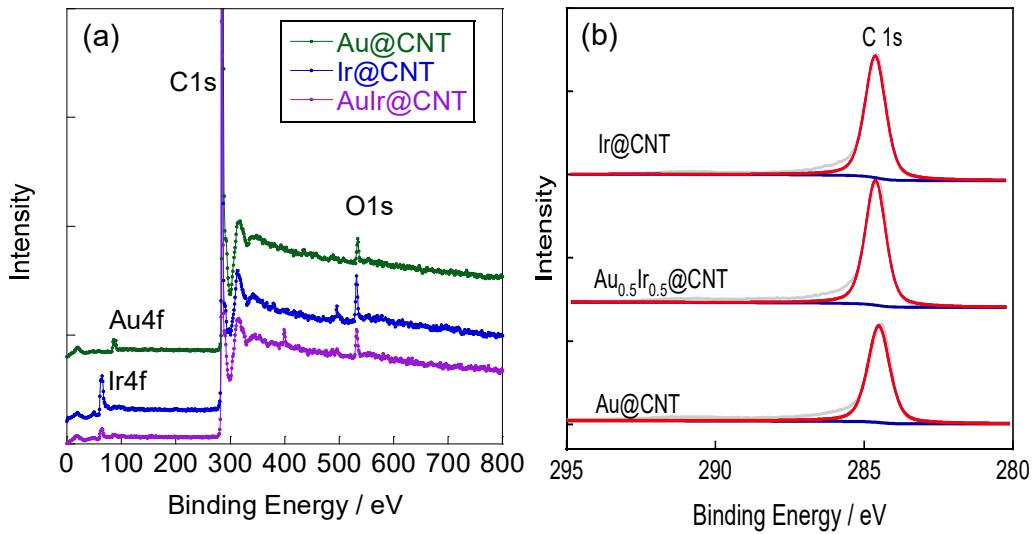
Figure S2 (a) XPS survey scan calibrated C1s peaks (b) of Au@CNT, $Au_{0.5}Ir_{0.5}$@CNT and Ir@CNT electrocatalysts.
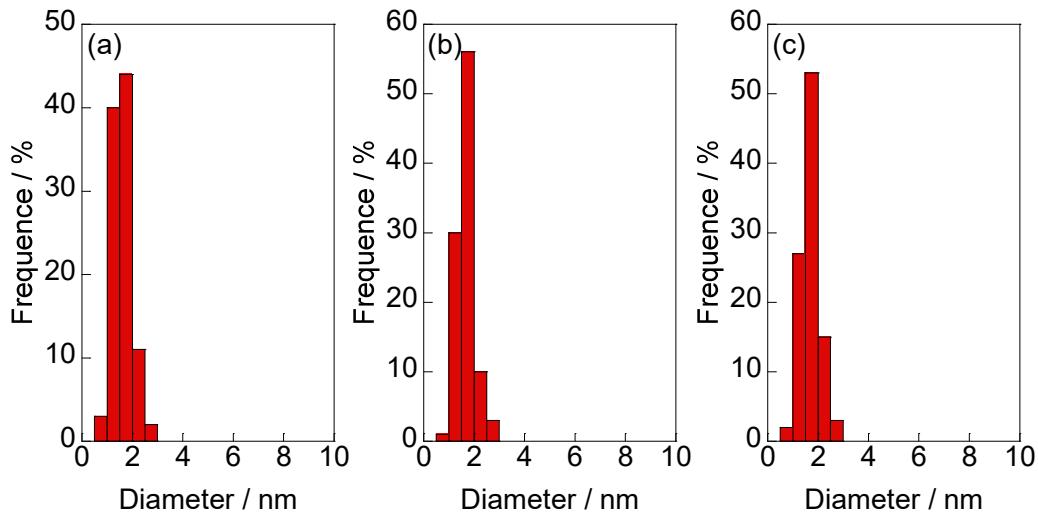
Figure S3 Histrograms of size distributions of Au@CNT (a), Ir@CNT (b) and $Au_{0.5}Ir_{0.5}$@CNT (c) electrocatalysts.
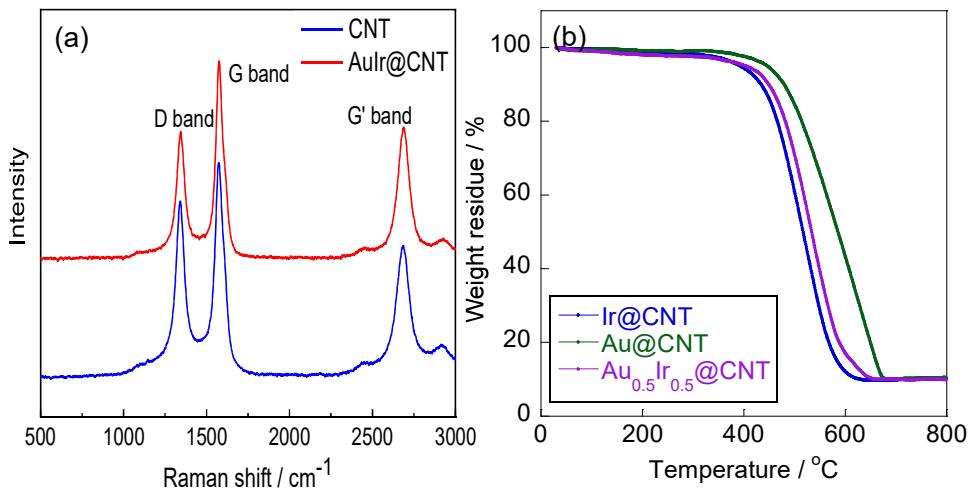
Figure S4 (a) Raman spectroscopies of CNT and $Au_{0.5}Ir_{0.5}$@CNT. (b) TGA curves of Au@CNT, Ir@CNT and $Au_{0.5}Ir_{0.5}$@CNT electrocatalysts recorded from room temperature to 800 °C under air flow.
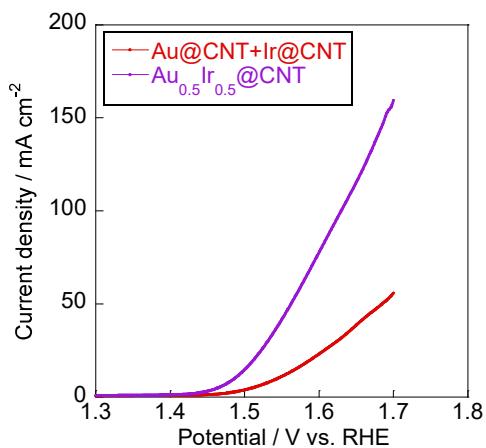
Figure S5 OER performance of $Au_{0.5}Ir_{0.5}$@CNT and physical mixed Au@CNT/Ir@CNT (1:1) in 0.5 M H_2SO_4 electrolyte.
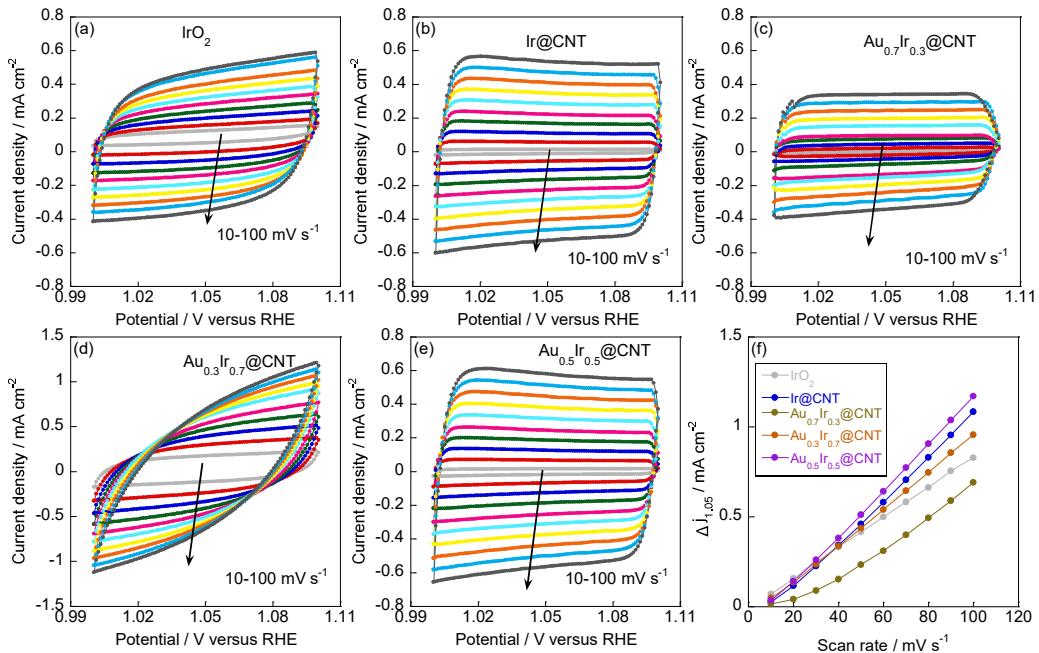
Figure S6 Cyclic voltammetry curves recorded for IrO_2 (a), Ir@CNT (b), $Au_{0.7}Ir_{0.3}$@CNT (c), $Au_{0.3}Ir_{0.7}$@CNT (d) and $Au_{0.5}Ir_{0.5}$@CNT (e) with various scan rates. (f) Calculated double-layer capacitances of various electrocatalysts.
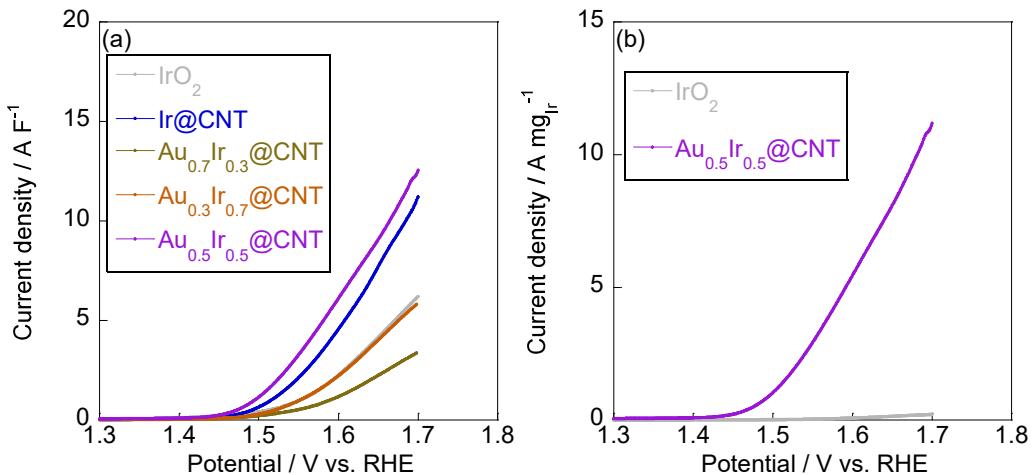
Figure S7 Specific (a) and mass (b) activities of IrO_2, Ir@CNT, $Au_{0.7}Ir_{0.3}$@CNT, $Au_{0.3}Ir_{0.7}$@CNT and $Au_{0.5}Ir_{0.5}$@CNT electrocatalysts.
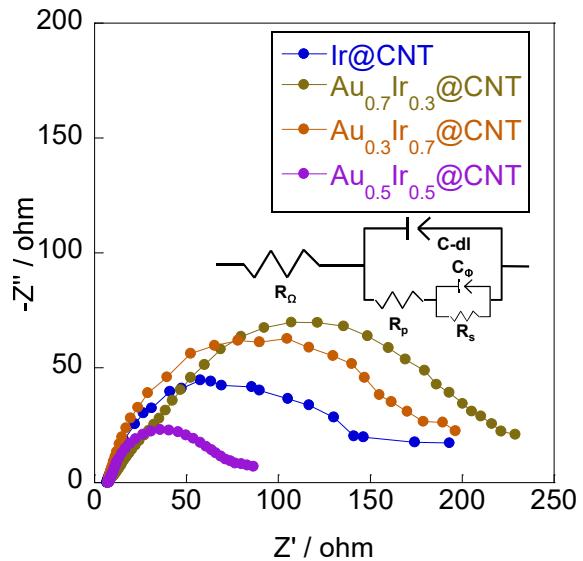
Figure S8 Electrochemical impedance spectroscopies of Ir@CNT, Au$_{0.7}$Ir$_{0.3}$@CNT, Au$_{0.3}$Ir$_{0.7}$@CNT and Au$_{0.5}$Ir$_{0.5}$@CNT electrocatalysts.
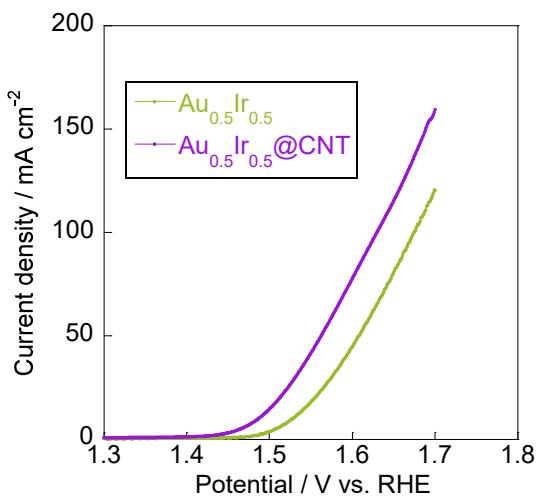
Figure S9 OER performance of unsupported Au$_{0.5}$Ir$_{0.5}$ and Au$_{0.5}$Ir$_{0.5}$@CNT electrocatalyst.
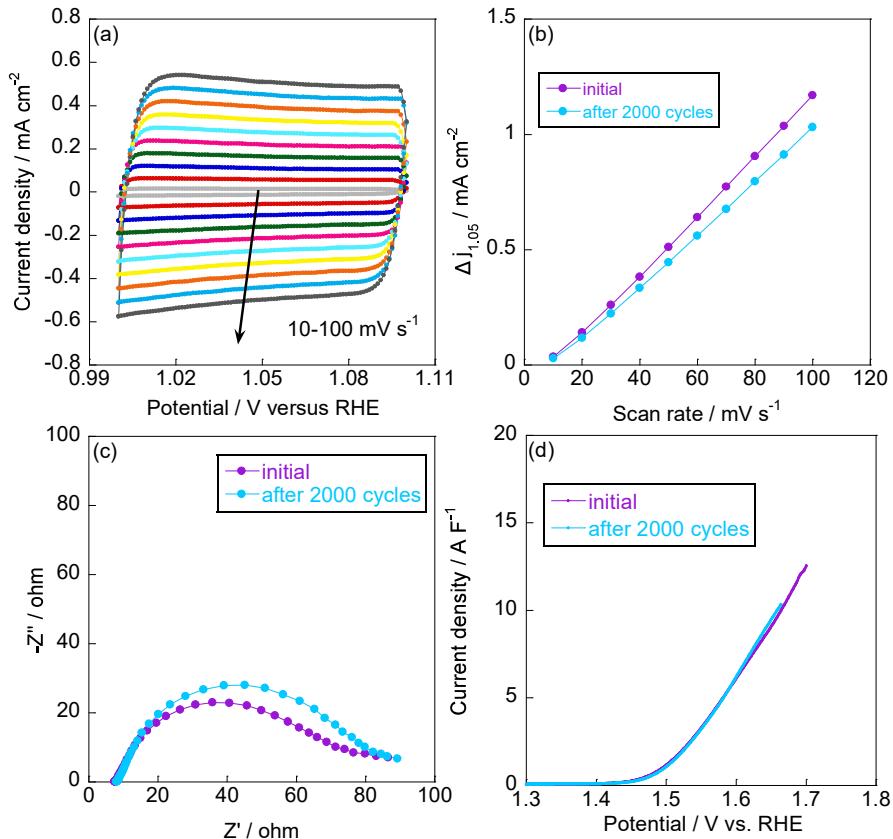
Figure S10 Cyclic voltammetry curves (a), double-layer capacitances (b), electrochemical impedance spectroscopies (c) and specific activities (d) of $Au_{0.5}Ir_{0.5}@CNT$ electrocatalyst after 2000 potential cycles.
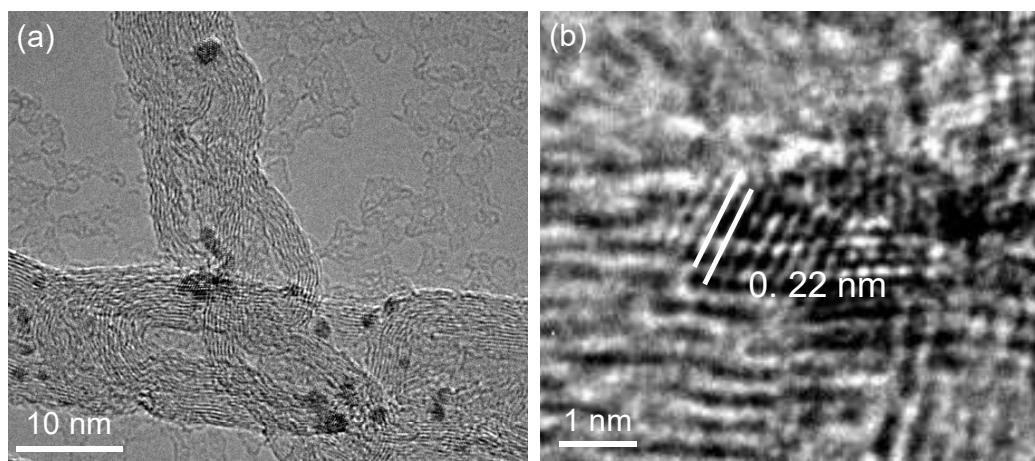
Figure S11 TEM (a) and HR-TEM (b) images of $Au_{0.5}Ir_{0.5}@CNT$ electrocatalyst after 2000 potential cycles.
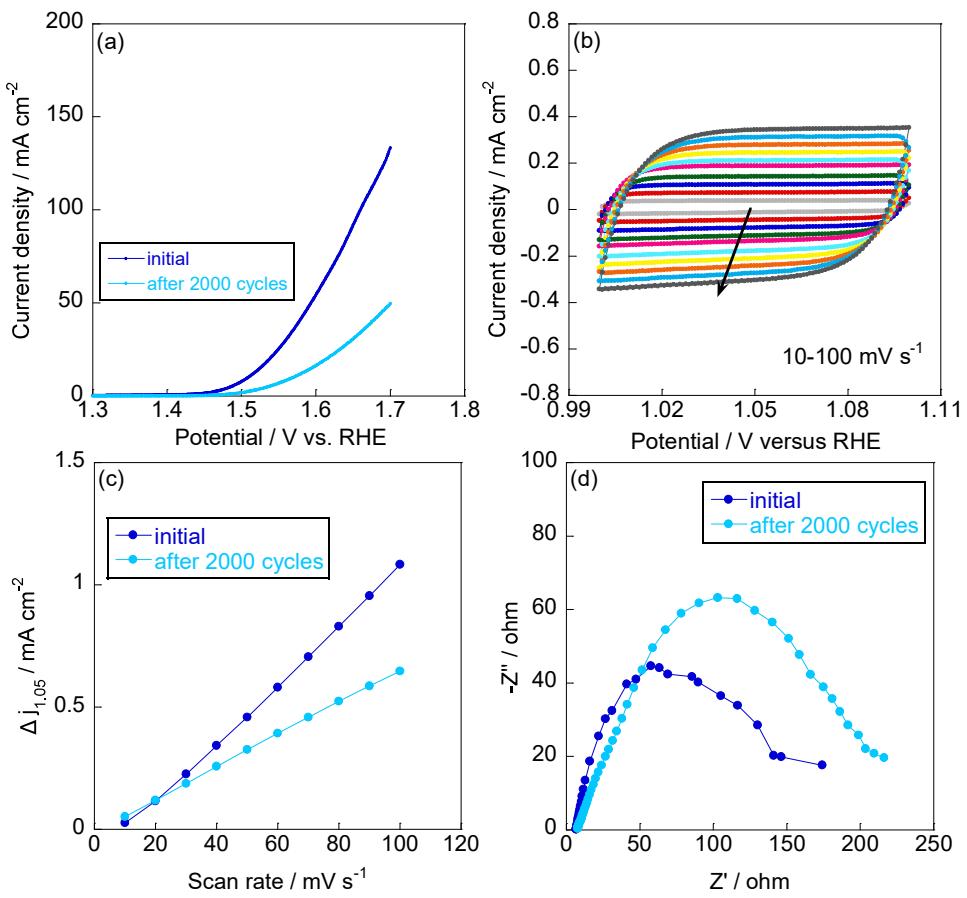
Figure S12 OER performance (a), cyclic voltammetry curves (b), double-layer capacitances (c) and electrochemical impedance spectroscopies (d) of Ir@CNT electrocatalyst after 2000 potential cycles.
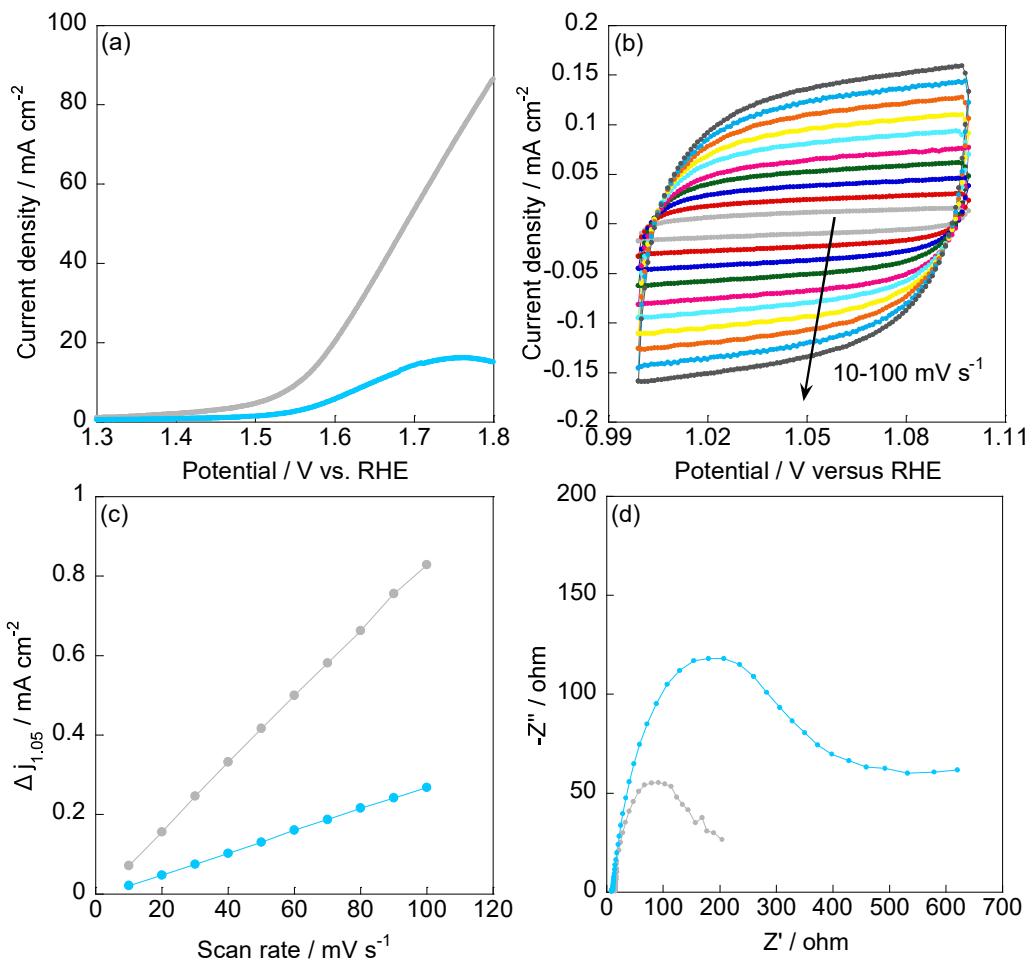
Figure S13 OER performance (a), cyclic voltammetry curves (b), double-layer capacitances (c) and electrochemical impedance spectroscopies (d) of commercial IrO$_2$ electrocatalyst after 1000 potential cycles.
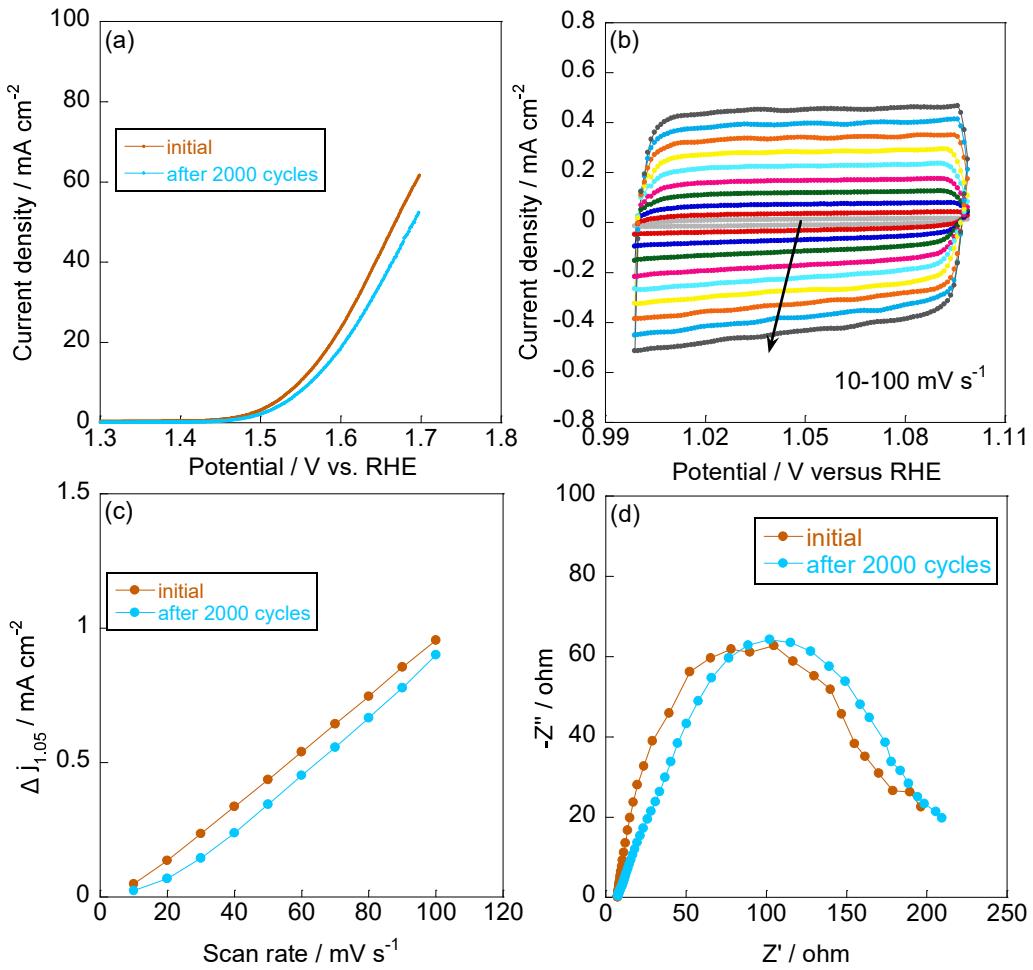
Figure S14 OER performance (a), cyclic voltammetry curves (b), double-layer capacitances (c) and electrochemical impedance spectroscopies (d) of $Au_{0.3}Ir_{0.7}$@CNT electrocatalyst after 2000 potential cycles.
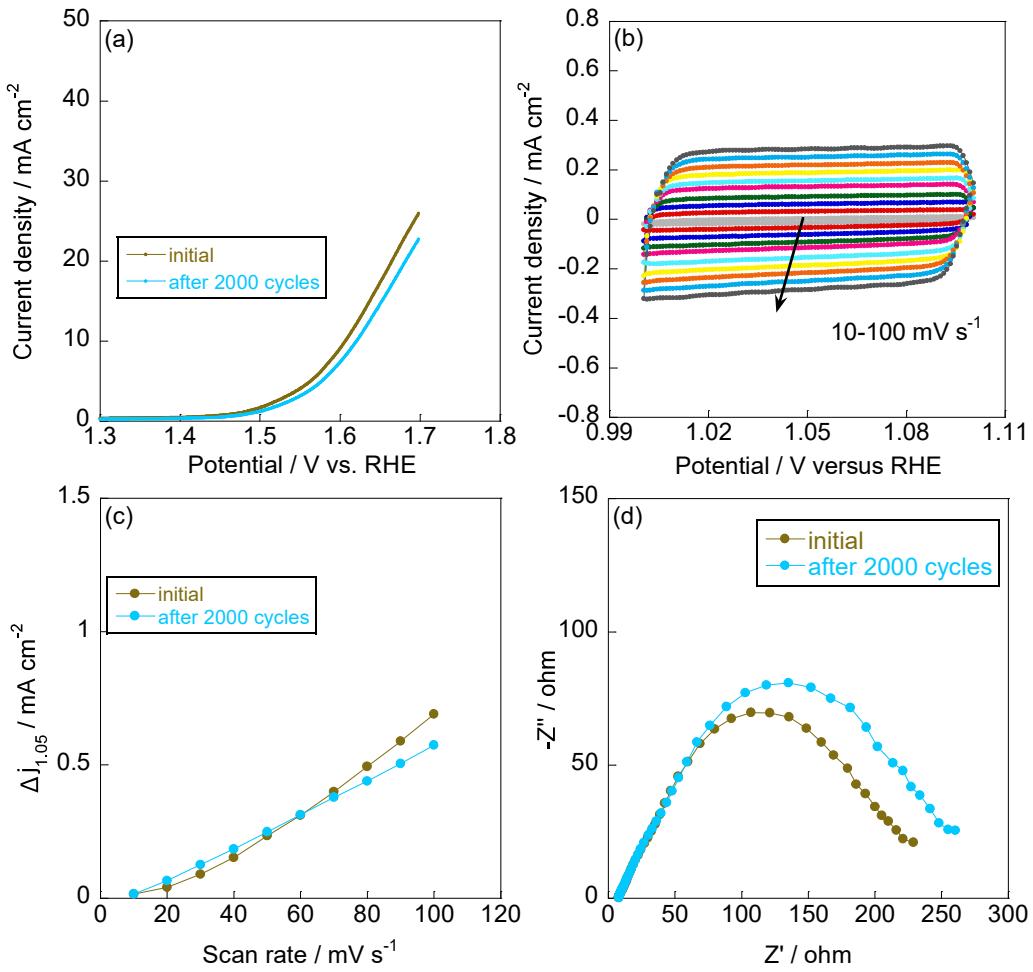
Figure S15 OER performance (a), cyclic voltammetry curves (b), double-layer capacitances (c) and electrochemical impedance spectroscopies (d) of $Au_{0.7}Ir_{0.3}@CNT$ electrocatalyst after 2000 potential cycles.
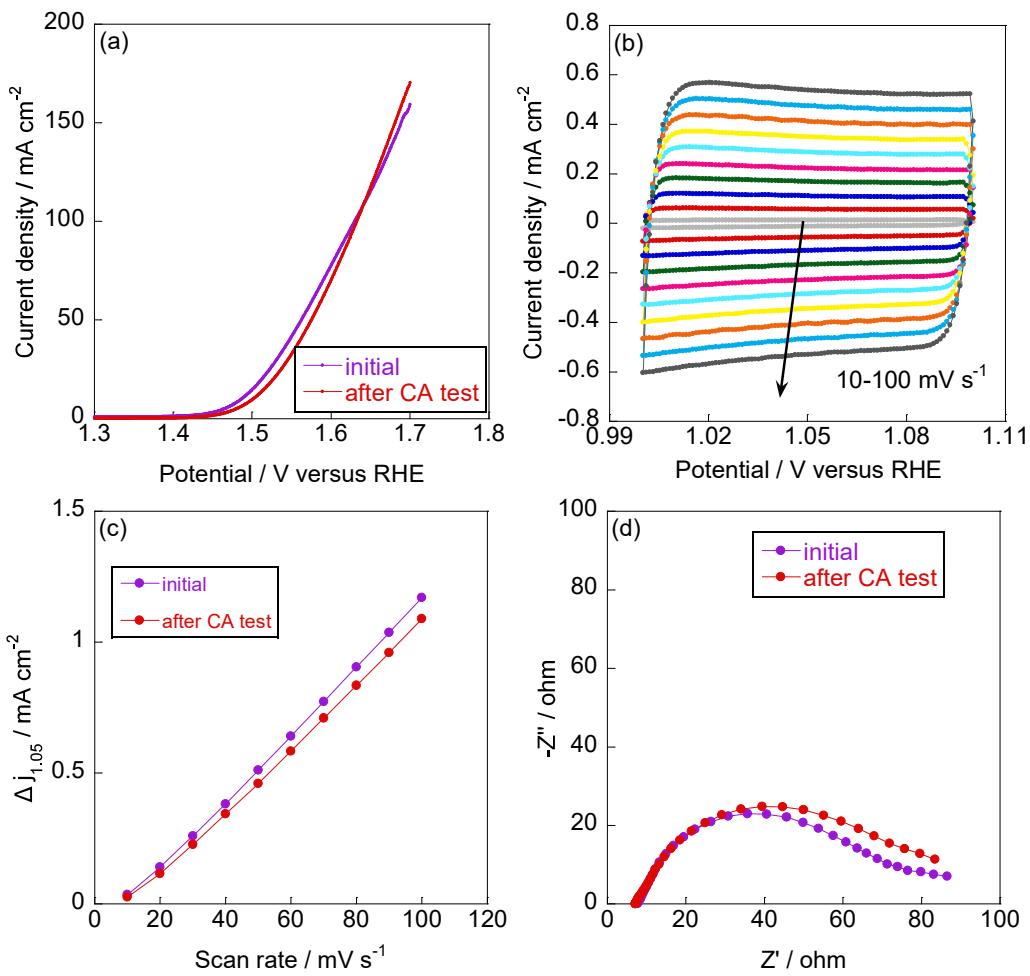
Figure S16 OER performance (a), cyclic voltammetry curves (b), double-layer capacitances (c) and electrochemical impedance spectroscopies (d) of $Au_{0.5}Ir_{0.5}@CNT$ electrocatalyst after CA test.
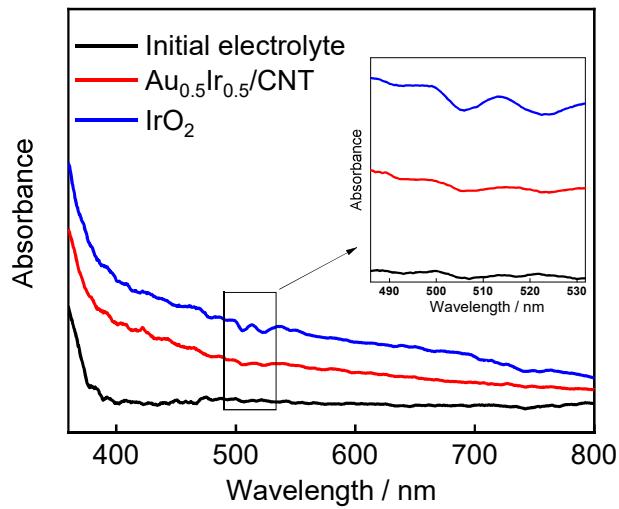
Figure S17 UV-vis spectroscopies of electrolytes after OER catalysis driven by commercial IrO_2 and $Au_{0.5}Ir_{0.5}$@CNT.
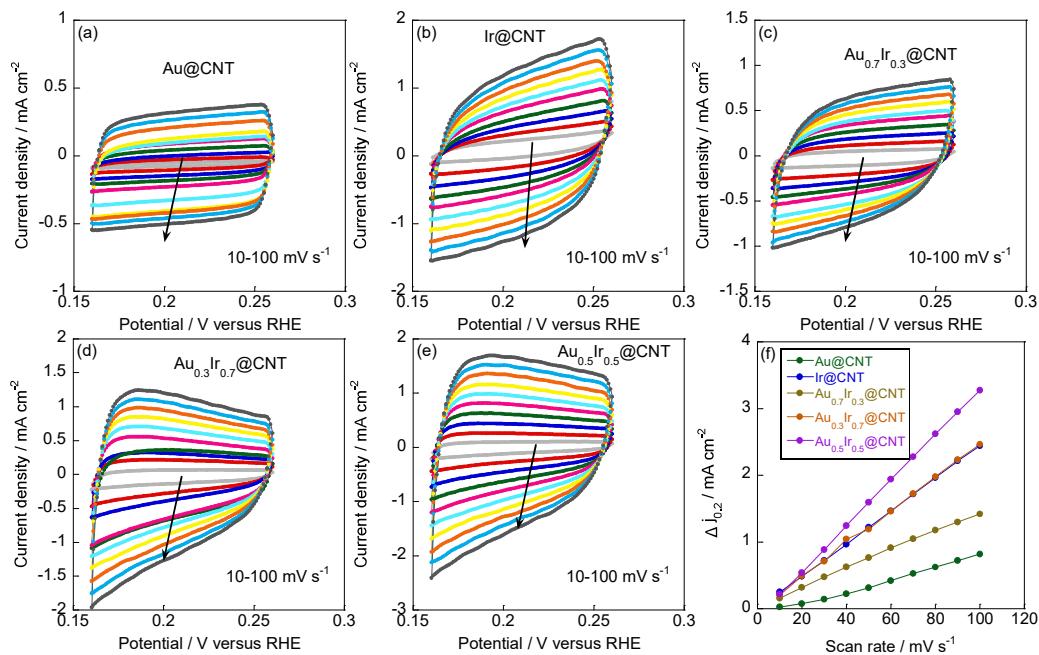
Figure S18 Cyclic voltammetry curves recorded for Au@CNT (a), Ir@CNT (b), $Au_{0.7}Ir_{0.3}$@CNT (c), $Au_{0.3}Ir_{0.7}$@CNT (d) and $Au_{0.5}Ir_{0.5}$@CNT (e) with various scan rates. (f) Calculated double-layer capacitances of various electrocatalysts.
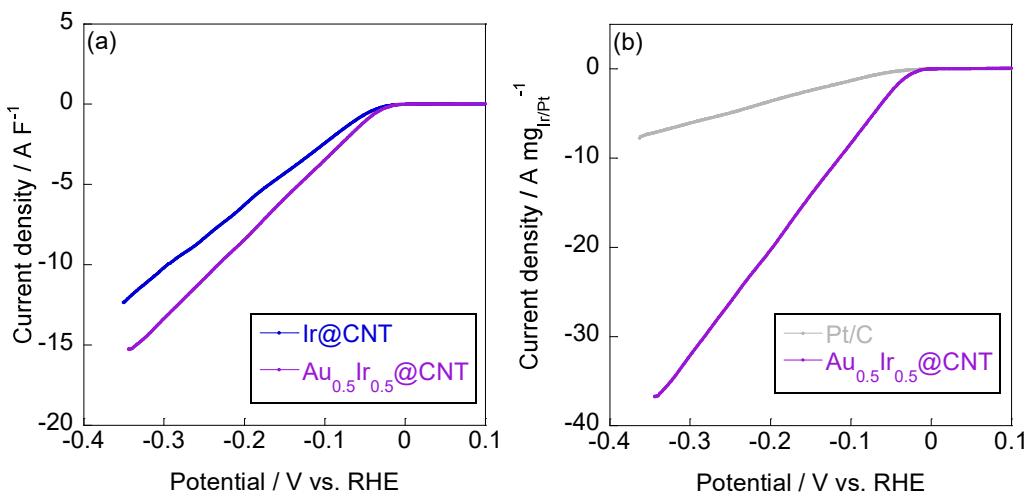
Figure S19 Specific activity of Ir@CNT and $Au_{0.5}Ir_{0.5}$@CNT. Mass activity of Pt/C and $Au_{0.5}Ir_{0.5}$@CNT.
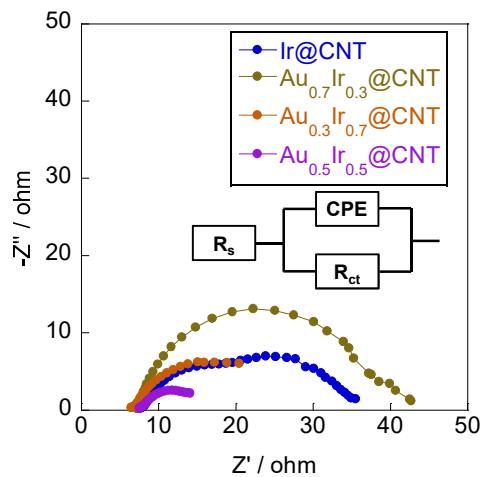
Figure S20 Electrochemical impedance spectroscopies of Ir@CNT, $Au_{0.7}Ir_{0.3}$@CNT, $Au_{0.3}Ir_{0.7}$@CNT and $Au_{0.5}Ir_{0.5}$@CNT electrocatalysts.
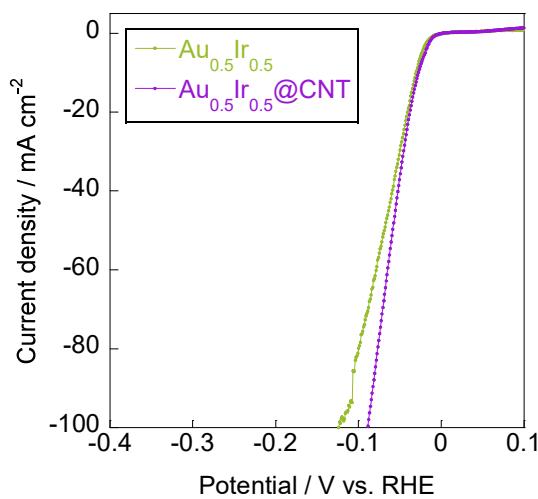
**Figure S21** HER performance of unsupported $Au_{0.5}Ir_{0.5}$ and $Au_{0.5}Ir_{0.5}@CNT$ electrocatalyst.
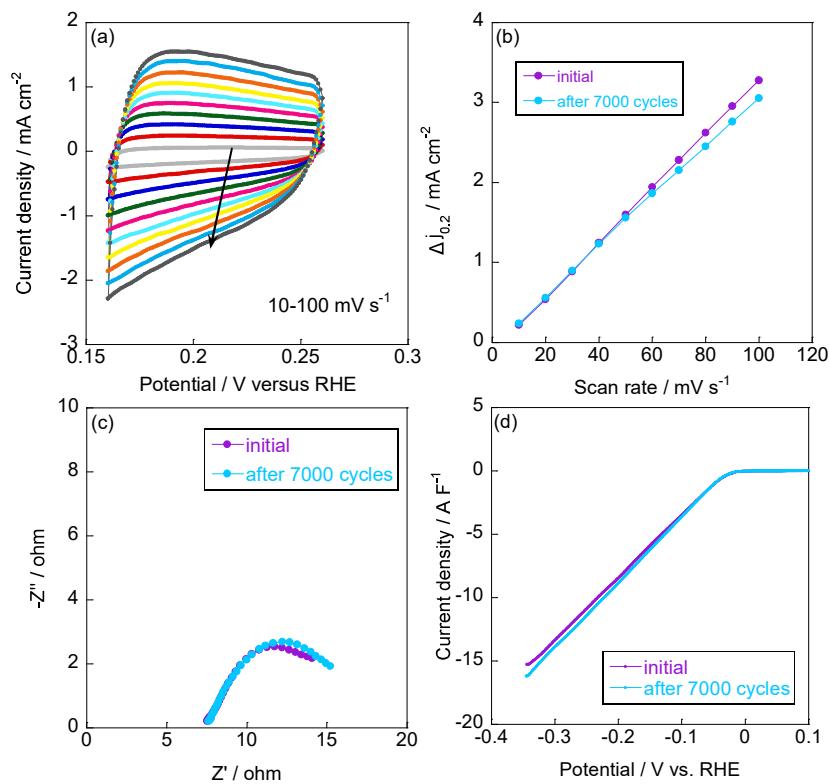
Figure S22 Cyclic voltammetry curves (a), double-layer capacitances (b), electrochemical impedance spectroscopies (c) and specific activities (d) of $Au_{0.5}Ir_{0.5}@CNT$ electrocatalyst after 7000 potential cycles.
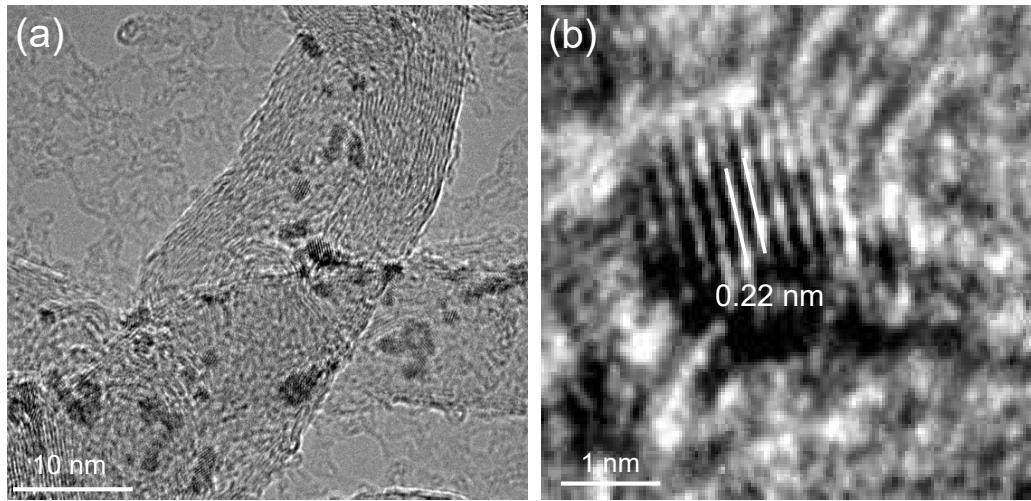
**Figure S23** TEM (a) and HR-TEM (b) images of Au$_{0.5}$Ir$_{0.5}$@CNT electrocatalyst after 7000 potential cycles.
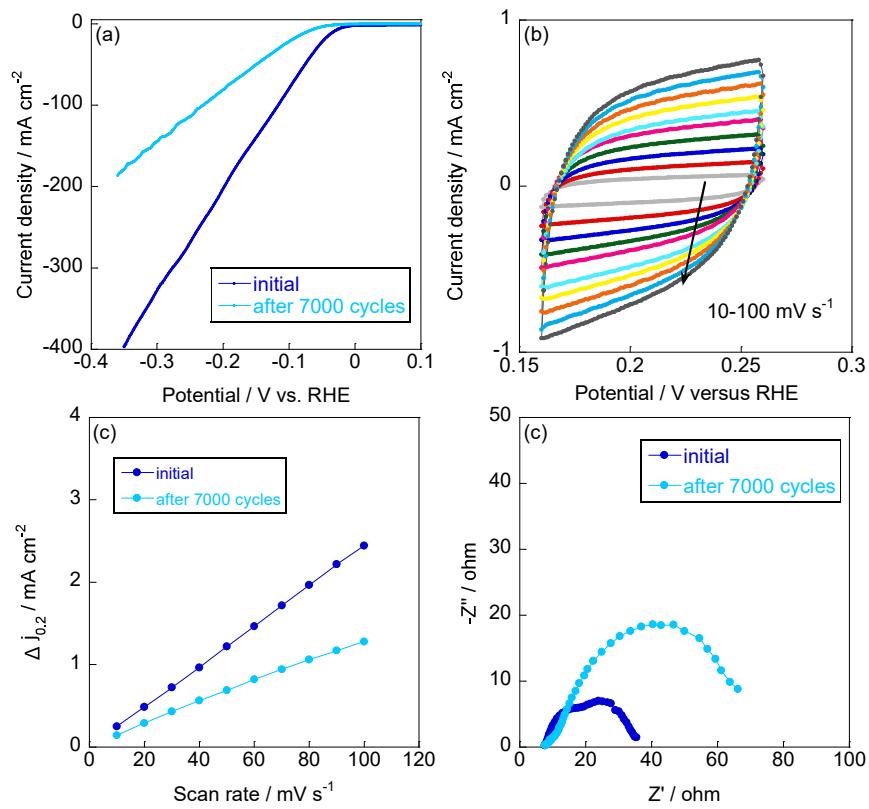

Figure S24 HER performance (a), cyclic voltammetry curves (b), double-layer capacitances (c) and electrochemical impedance spectroscopies (d) of Ir@CNT electrocatalyst after 7000 potential cycles.
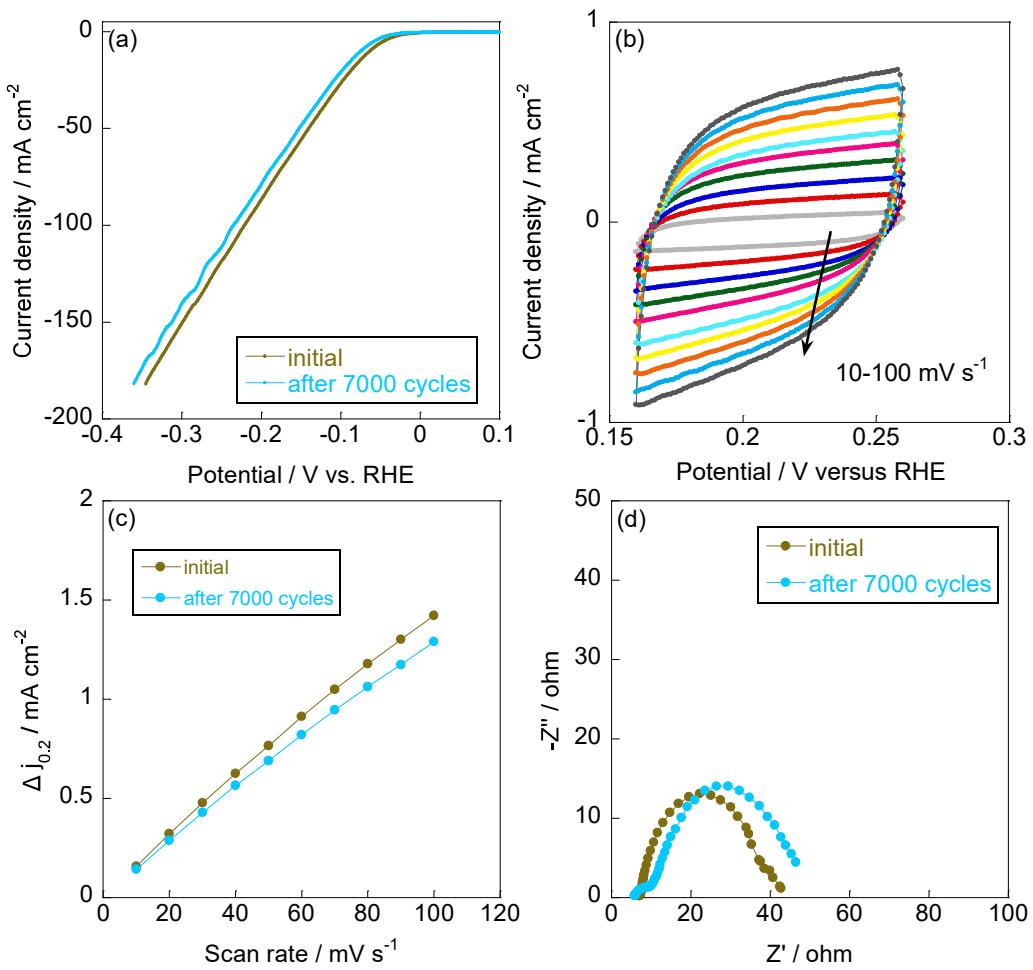
Figure S25 HER performance (a), cyclic voltammetry curves (b), double-layer capacitances (c) and electrochemical impedance spectroscopies (d) of Au$_{0.7}$Ir$_{0.3}$@CNT electrocatalyst after 7000 potential cycles.
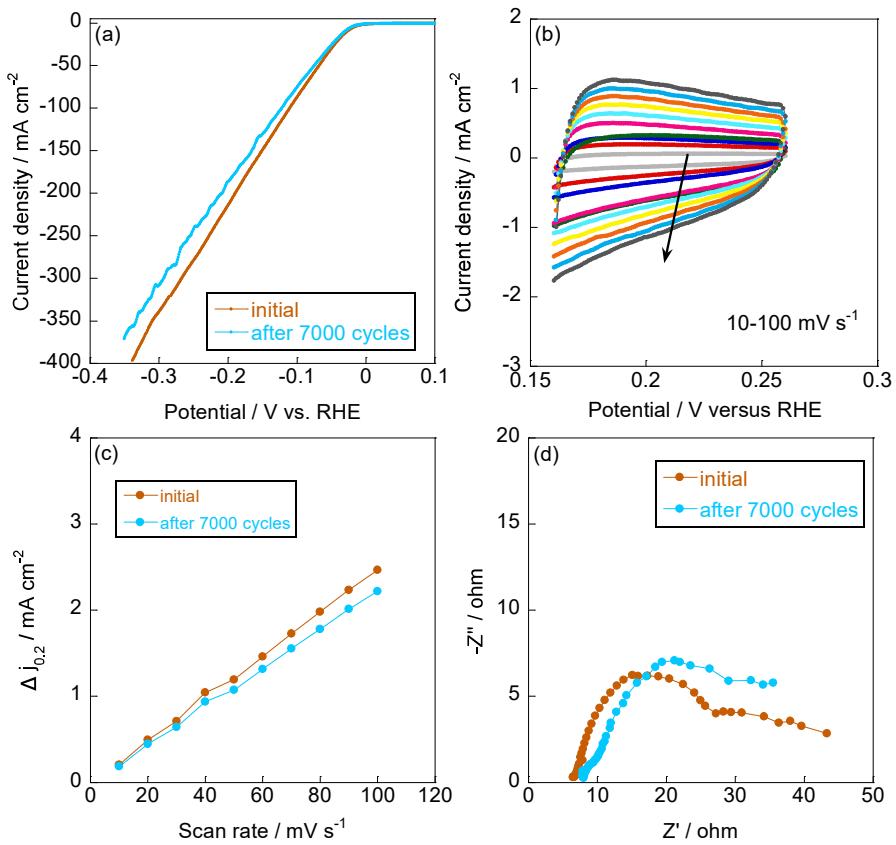
Figure S26 HER performance (a), cyclic voltammetry curves (b), double-layer capacitances (c) and electrochemical impedance spectroscopies (d) of $Au_{0.3}Ir_{0.7}$@CNT electrocatalyst after 7000 potential cycles.
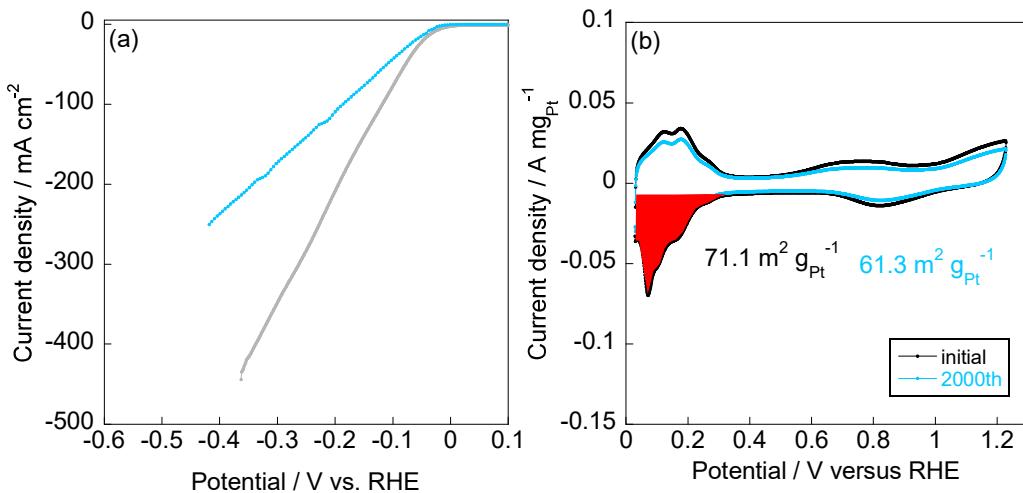

**Figure S27** HER performance (a) and ECSA (b) of commercial Pt/C before and after 2000 potential cycles.
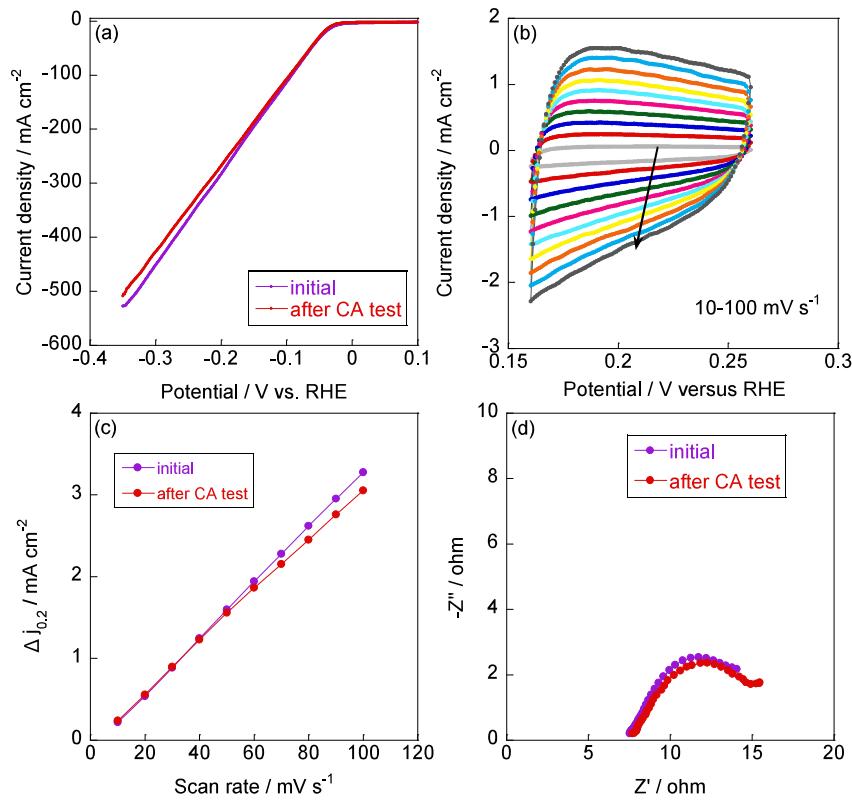
Figure S28 HER performance (a), cyclic voltammetry curves (b), double-layer capacitances (c) and electrochemical impedance spectroscopies (d) of $Au_{0.5}Ir_{0.5}$@CNT electrocatalyst after CA test.
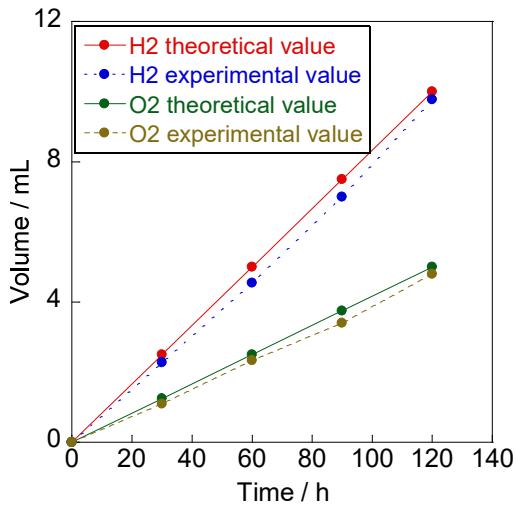

Figure S29 theoretical and experimental values of H_2 and O_2 collected from water splitting driven by $Au_{0.5}Ir_{0.5}$@CNT electrocatalyst.
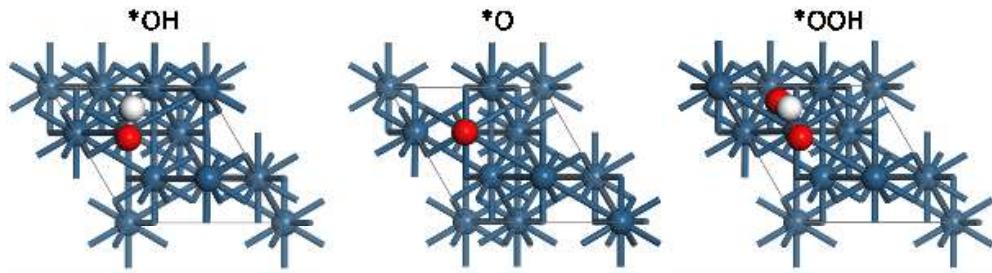
Figure S30 Structures of the intermediates in OER on Ir(111) surface.
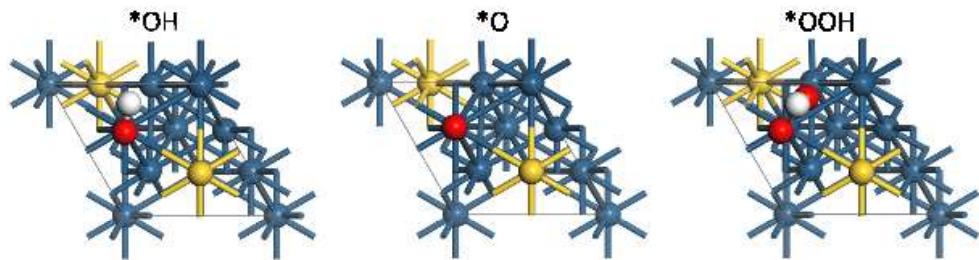

Figure S31 Structures of the intermediates in OER on AuIr(111) surface.

References

1. X. Liang, L. Shi, Y. Liu, H. Chen, R. Si, W. Yan, Q. Zhang, G.-D. Li, L. Yang and X. Zou, *Angew. Chem. Int. Ed.*, 2019, **58**, 7631-7635.

2. J. Gao, C.-Q. Xu, S.-F. Hung, W. Liu, W. Cai, Z. Zeng, C. Jia, H. M. Chen, H. Xiao, J. Li, Y. Huang and B. Liu, *J. Am. Chem. Soc.*, 2019, **141**, 3014-3023.

3. J. Shan, C. Guo, Y. Zhu, S. Chen, L. Song, M. Jaroniec, Y. Zheng and S.-Z. Qiao, *Chem*, 2019, **5**, 445-459.

4. H.-S. Oh, H. N. Nong, T. Reier, A. Bergmann, M. Gliech, J. Ferreira de Araújo, E. Willinger, R. Schlögl, D. Teschner and P. Strasser, *J. Am. Chem. Soc.*, 2016, **138**, 12552-12563.

5. Y. Pi, J. Guo, Q. Shao and X. Huang, *Chem. Mater.*, 2018, **30**, 8571-8578.

6. J. Zhu, Z. Chen, M. Xie, Z. Lyu, M. Chi, M. Mavrikakis, W. Jin and Y. Xia, *Angew. Chem. Int. Ed.*, 2019, **58**, 7244-7248.

7. F. Lv, J. Feng, K. Wang, Z. Dou, W. Zhang, J. Zhou, C. Yang, M. Luo, Y. Yang, Y. Li, P. Gao and S. Guo, *ACS Cent. Sci.*, 2018, **4**, 1244-1252.

8. H. Jin, Y. Hong, J. Yoon, A. Oh, N. K. Chaudhari, H. Baik, S. H. Joo and K. Lee, *Nano Energy*, 2017, **42**, 17-25.

9. B. Jiang, Y. Guo, J. Kim, A. E. Whitten, K. Wood, K. Kani, A. E. Rowan, J. Henzie and Y. Yamauchi, *J. Am. Chem. Soc.*, 2018, **140**, 12434-12441.

10. S.-H. Cho, K. R. Yoon, K. Shin, J.-W. Jung, C. Kim, J. Y. Cheong, D.-Y. Youn, S. W. Song, G. Henkelman and I.-D. Kim, *Chem. Mater.*, 2018, **30**, 5941-5950.

11. J. Shan, T. Ling, K. Davey, Y. Zheng and S.-Z. Qiao, *Adv. Mater.*, 2019, **31**, 1900510.

12. L. Fu, F. Yang, G. Cheng and W. Luo, *Nanoscale*, 2018, **10**, 1892-1897.